


Response of CR-39 nuclear track detectors to protons with non-normal incidence

Cite as: Rev. Sci. Instrum. **92**, 013504 (2021); <https://doi.org/10.1063/5.0029230>

Submitted: 10 September 2020 . Accepted: 16 December 2020 . Published Online: 08 January 2021

 R. Przybocki,  M. Gatu Johnson, G. Sutcliffe, B. Lahmann, F. H. Seguin,  J. Frenje,  P. Adrian,  T. M. Johnson, J. Percy,  N. V. Kabadi,  A. Birkel, and  R. D. Petraso



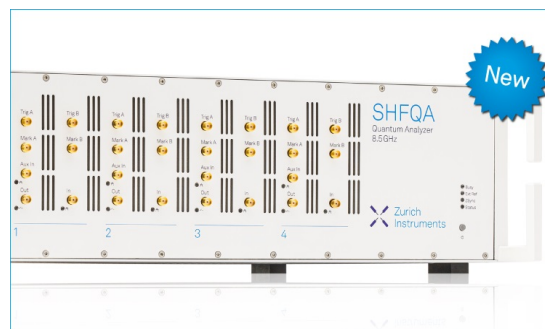
View Online



Export Citation



CrossMark



Your Qubits. Measured.

Meet the next generation of quantum analyzers

- Readout for up to 64 qubits
- Operation at up to 8.5 GHz, mixer-calibration-free
- Signal optimization with minimal latency

Find out more



Response of CR-39 nuclear track detectors to protons with non-normal incidence

Cite as: Rev. Sci. Instrum. 92, 013504 (2021); doi: 10.1063/5.0029230

Submitted: 10 September 2020 • Accepted: 16 December 2020 •

Published Online: 8 January 2021



R. Przybocki,^{a)} M. Gatu Johnson, G. Sutcliffe, B. Lahmann, F. H. Seguin, J. Frenje, P. Adrian,
T. M. Johnson, J. Pearcy, N. V. Kabadi, A. Birkel, and R. D. Petrasso

AFFILIATIONS

Plasma Science and Fusion Center, Massachusetts Institute of Technology, Cambridge, Massachusetts 02139, USA

^{a)} Author to whom correspondence should be addressed: ryanprzybocki@alum.mit.edu

ABSTRACT

This paper presents data from experiments with protons at non-normal incidence to CR-39 nuclear track detectors, analyzing the properties of detection efficiency, proton track diameter, track contrast, and track eccentricity. Understanding the CR-39 response to protons incident at an angle is important for designing charged particle detectors for inertial confinement fusion (ICF) applications. This study considers protons with incident energies less than 3 MeV. In this regime, an incident angle of 10° has no effect on CR-39 detection efficiency, and $>85\%$ detection efficiency is preserved up through 25° in the range of 1.0 MeV–2.1 MeV. For ICF applications, incident angles above 30° are deemed impractical for detector design due to significant drops in proton detection at all energies. We observe significant reductions in detection efficiency compared to theoretical predictions, particularly at low energies where proton tracks are etched away. The proton track diameter measured by the scan system is observed to decrease with higher incident angles. The track diameters are analyzed with two fitting models, and it is shown that the diameter–energy relation can be fit with the existing models at angles up to 30° . The optical contrast of the tracks tends to increase with the angle, meaning that the tracks are fainter, and a larger increase is observed for higher energies. Eccentricity, a measure of how elongated proton tracks are, increases with the incident angle and drops after the critical angle. The lowest energy tracks remain nearly circular even at higher angles.

Published under license by AIP Publishing. <https://doi.org/10.1063/5.0029230>

I. INTRODUCTION

Solid state nuclear track detectors made from CR-39 plastic are used at Inertial Confinement Fusion (ICF) facilities such as Omega,¹ Z,² and the National Ignition Facility (NIF).^{3–5} At these facilities, detector insensitivity to background radiation such as x rays and electromagnetic noise is paramount, so the detection through mechanical means such as CR-39 is preferred as it avoids the background problems associated with electromagnetic detectors.

When an energetic charged particle collides with CR-39, it damages molecular chains leaving behind a characteristic track. The tracks are revealed through chemical etching with NaOH, which removes the material on the surface of the detector as well as inside the tracks. The rate at which tracks are etched (“track etch velocity”) is faster than the rate at which the rest of the plastic is etched (“bulk etch velocity”), so the tracks are visible after etching as more track

material is removed than the surrounding material. These tracks in the plastic vary in diameter and depth, in relation to the rate at which the incident particles lose energy, dE/dx . Detailed discussions of the physics behind proton registration in CR-39 and the associated chemical etching process were given by Hermsdorf⁶ and Dörschel *et al.*⁷

The detection efficiency of CR-39 is defined as the ratio of the number of incident particles experimentally detected by the CR-39 to the number expected. Seguin *et al.* gave a CR-39 proton detection efficiency of 100% for incident energies between about 0.5 MeV and 6 MeV.⁵ However, these observations for detection efficiency were made for protons at normal incidence to the CR-39, and the response to protons in this energy range incident at an angle has not been well characterized. Also uncertain is how non-normal incidence affects other properties of CR-39 tracks, such as diameter, optical contrast, and track roundness. Certain simplifications to the analysis of normally incident particles are not possible when

the particles are incident at an angle, such as automatically filtering out non-circular tracks that usually only appear as background noise.

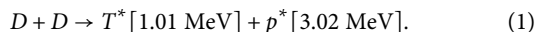
Previously, Stafford *et al.* examined the non-normal detection efficiency for protons incident between 3 MeV and 10 MeV using a single CR-39 etch time of 16 h.⁸ Frenje *et al.* also simulated the CR-39 response to non-normal incidence of recoil protons from neutron collisions.⁹ As an example of an application where a better understanding of CR-39 response under angled incidence is important, we consider D–D neutron spectrometer designs proposed by Lahmann *et al.*¹⁰ Both designs involve incident neutrons passing through a conversion foil and colliding elastically with ions and scattering protons at an angle. These recoil protons reach a CR-39 detector at a non-normal incident angle, so characterizing the CR-39 response to non-normal incidence protons is essential for inferring neutron spectra in such a device.

In this paper, we present results from a study where CR-39 is exposed to protons up to 3 MeV while systematically varying the angle of incidence in increments from 0° to 50°. The detection efficiency and track characteristics (diameter, contrast, and roundness) as a function of angle are discussed. This paper is organized as follows. In Sec. II, the experimental setup is described. In Sec. III, the analysis methods for detection efficiency are explained. In Sec. IV, the results are discussed, focusing, in turn, on efficiency, track diameter as a function of energy, contrast, and eccentricity. Finally, Sec. V concludes this paper.

II. EXPERIMENTAL DESIGN

The experiments in this paper were carried out at the Massachusetts Institute of Technology (MIT) in the Linear Electrostatic Ion Accelerator (LEIA), a facility that develops diagnostics for Omega, Z, and the NIF.¹¹ In our experiments, a high voltage (125 kV) accelerates deuterium ions down the beam line and onto an Erbium-Deuteride (ErD₂) target in order to produce D–D fusion products. Ports extending off the target chamber allow the placement of CR-39 detectors for experiments. The target chamber, extension ports, and CR-39 holder are shown in Fig. 1.

The branch of the D–D fusion reaction of interest is as follows:



This reaction branch yields a proton with an energy of 3.02 MeV. We can study energy values at or below this value by introducing range filters that reduce the kinetic energy of these protons. We choose a simple step range filter (SRF) design, which implements fixed aluminum foil thicknesses to downshift the protons to energies below 3 MeV on CR-39. We refer to these aluminum foil arrangements as “filters.” To limit the number of independent trials we need, the filter arrangement includes six individual aluminum filters ovetop one 5 cm diameter piece of CR-39. A schematic for the filter design is shown in Fig. 2.

The post-filter energies were calibrated with a Silicon Surface Barrier Detector (SBD) in the LEIA target chamber. The mean energy measured behind each filter is given in Table I. As shown in Table I, the measured spectra had nonzero standard deviations σ , so the incident protons were not perfectly monoenergetic.

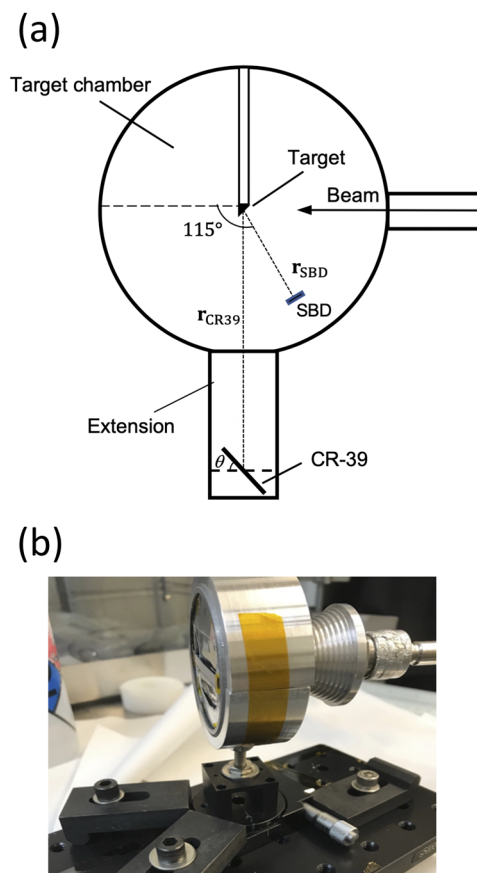


FIG. 1. Setup of the experiment. (a) Top view of the accelerator chamber, showing the beam line, the target, and the positions of the SBD and CR-39 detector. (b) The rotating CR-39 enclosure mounted on the pedestal that is placed in the extension chamber.

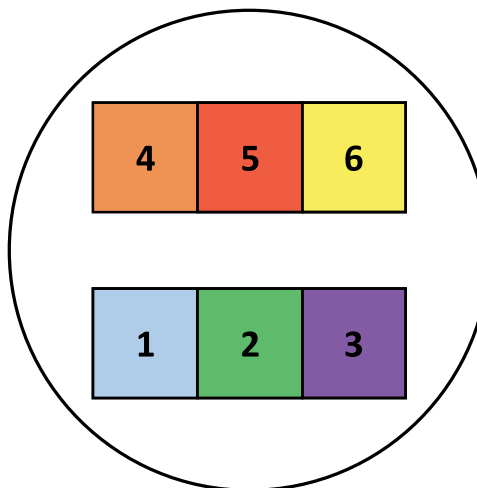


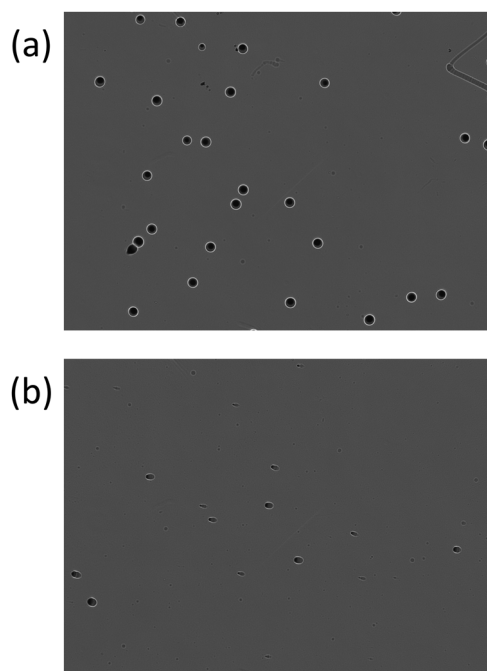
FIG. 2. Schematic for the filter arrangement that includes six different aluminum thicknesses. Filters are numbered 1 through 6 in order of increasing thickness. Filter thicknesses are listed in Table I.

TABLE I. Filter numbers and their corresponding calibrated mean energies, energy distribution widths, and aluminum thicknesses as calculated by SRIM.

Filter	Mean energy (MeV)	σ (MeV)	Al thickness (μm)
1	2.898	0.056	5.36
2	2.471	0.069	22.87
3	2.063	0.086	37.72
4	1.668	0.103	50.29
5	1.201	0.127	62.75
6	0.740	0.141	72.35

A consistent experimental procedure is followed for all trials on CR-39 while only varying the angle offset of the CR-39. The filters are aligned with the rows (1–3) and (4–6) parallel to the base of the holding apparatus, and the CR-39 piece is held in place directly behind the filters. The platform holding the CR-39 is placed on tracks within the accelerator's extension that enables a consistent setup at the same distance each time. The accelerator is operated with a deuterium ion beam to produce 3.02 MeV protons as in Eq. (1). Experiments were performed at the following angles (in degrees): 0° , 10° , 20° , 25° , 30° , 35° , 40° , 45° , and 50° .

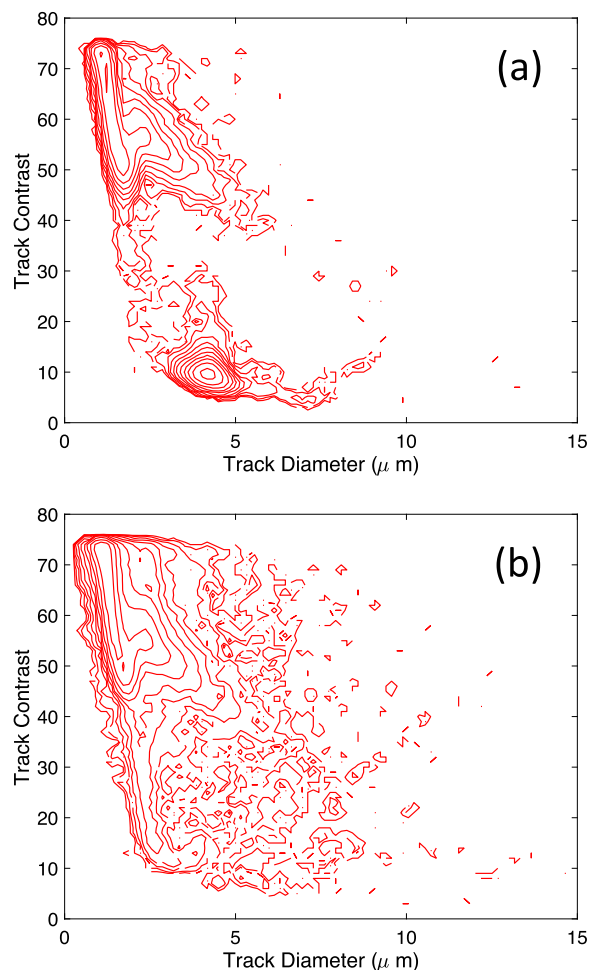
The CR-39 rounds are etched with 6N NaOH at 80°C for fixed durations of 2 h, 4 h, and 5 h and then scanned with an optical

**FIG. 3.** Sample microscopic images of CR-39 behind filter 3. Panel (a) shows the proton tracks at normal incidence, while panel (b) shows the tracks of protons incident at 30° , where the oblique shape of the tracks is visible. Both CR-39 pieces were etched for 2 h.

microscope. Example microscope frames of CR-39 are shown in Fig. 3. A computer program tabulates the CR-39 track properties from each experiment, including track density, diameter, contrast, and eccentricity. Proton track density (tracks/ cm^2) is used to determine proton flux on the CR-39. Contrast is defined in this experiment as (100%—optical contrast in %), i.e., the darkest proton tracks have the lowest contrast and vice versa. Eccentricity is a measure of the roundness of the tracks, with a higher value denoting a more oblique track.

III. ANALYSIS METHODS FOR DETECTION EFFICIENCY

A method is devised to compare the proton flux (tracks/ cm^2) across different CR-39 arrangements. To normalize these to a

**FIG. 4.** Example contour plots of track contrast vs diameter for a section of CR-39. In panel (a), note the well-defined contour peak at about $4\ \mu\text{m}$ on the top plot. This represents the signal that is easily separable from the higher contrast background noise, whereas in panel (b), the signal begins to blend with noise at higher contrasts.

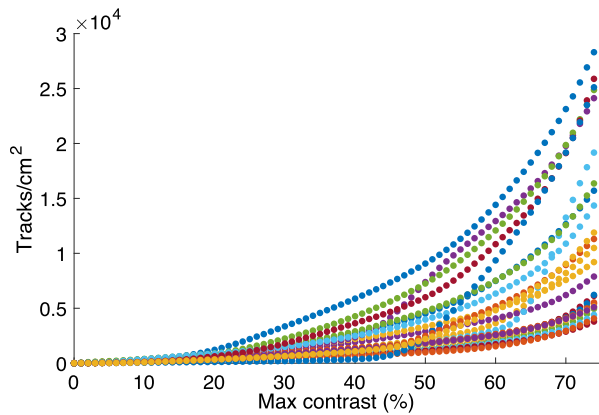


FIG. 5. Level of background noise in tracks/cm² at maximum contrast levels up to 75% across 24 separate CR-39 pieces.¹² Pieces were not exposed to ions prior to processing. Averaging across all pieces at a given contrast yields an uncertainty figure for the background tracks.

common baseline, we use the observed proton flux on the CR-39 and divide by the theoretical expected flux, which is determined from the SBD flux, adjusted for the different distances and orientations of the SBD and CR-39 detector. This number is the fraction detection in CR-39 relative to the SBD, which we call the detection efficiency. The SBD is expected to have a 100% detection efficiency for all proton energies of interest. This experiment aims for ~20 proton tracks in CR-39 per microscope frame to reflect the expected conditions in the proposed neutron spectrometers. This corresponds to roughly 16 700 tracks/cm² in CR-39, given a microscope frame area of 0.12 mm².

The theoretical expected flux is related to the SBD flux by the inverse square law. We also consider that the angle offset θ of CR-39 reduces its cross-sectional area available for incident protons by a factor of $\cos(\theta)$. Finally, we include a correction factor to account for the different angular positions of the SBD and the CR-39 detector. From the accelerator facility characterization data collected previously, the flux measured by an SBD at an angle of 115° (relative to the beam line) is 0.9676 times that of an SBD at 90° (the position of the CR-39 in this experiment).¹¹ Combining these contributions, we obtain the following relationship between the expected CR-39 flux (tracks/cm²) and observed SBD counts:

$$\Phi_{\text{expected}} = \frac{C_{\text{SBD}}}{A_{\text{SBD}}} \cdot \left(\frac{r_{\text{SBD}}}{r_{\text{CR39}}} \right)^2 \cdot \cos(\theta) \cdot \frac{1}{0.9676}, \quad (2)$$

where C_{SBD} is the number of counts observed on the SBD, A_{SBD} is the SBD aperture area (0.172 cm² in our experiment), and r_{SBD} and r_{CR39} are the distances from the target to the SBD and CR-39, respectively.

The main contribution to the error in our expected flux comes from the uncertainty in the two distance measurements, r_{SBD} and r_{CR39} . These were measured as $r_{\text{SBD}} = 177.2 \pm 2$ mm and $r_{\text{CR39}} = 628 \pm 5$ mm, making the error on the flux measurement 4%. This provides a lower bound for error bars when comparing the measured flux to expected flux for detection efficiency.

Tritons, which are also produced in the D–D reaction as shown in Eq. (1), do not interfere with the proton measurements presented here. Tritons are stopped by all filters, except the thinnest (filter 1) in our experiment. By placing suitable bounds on the track diameters, the proton tracks are isolated from the triton products for filter 1. For CR-39 arrangements that yield a significant number of high contrast (lighter colored) tracks, additional sources of error must be considered, specifically the large number of intrinsic background tracks that obfuscate the data. Typically, for reasonably low contrast

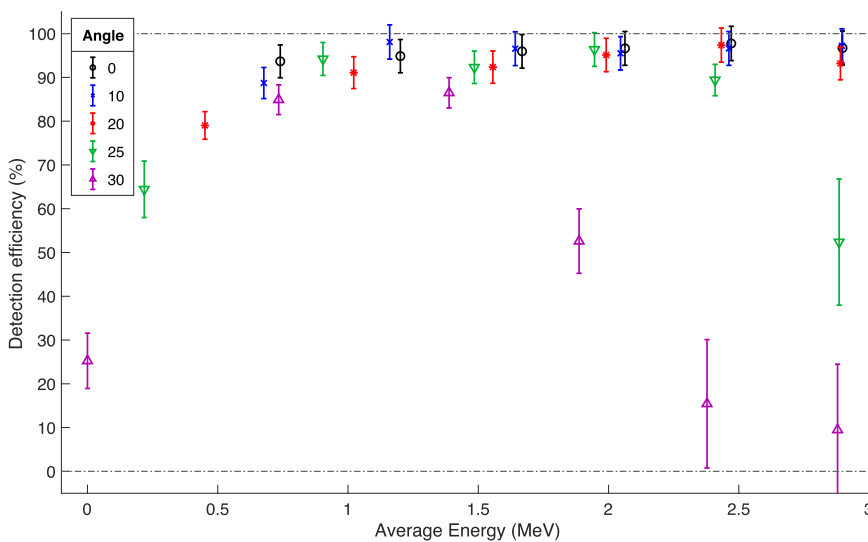


FIG. 6. Detection efficiency of CR-39 for a 2 h etch procedure vs incident energy, for incident angles up through 30°.

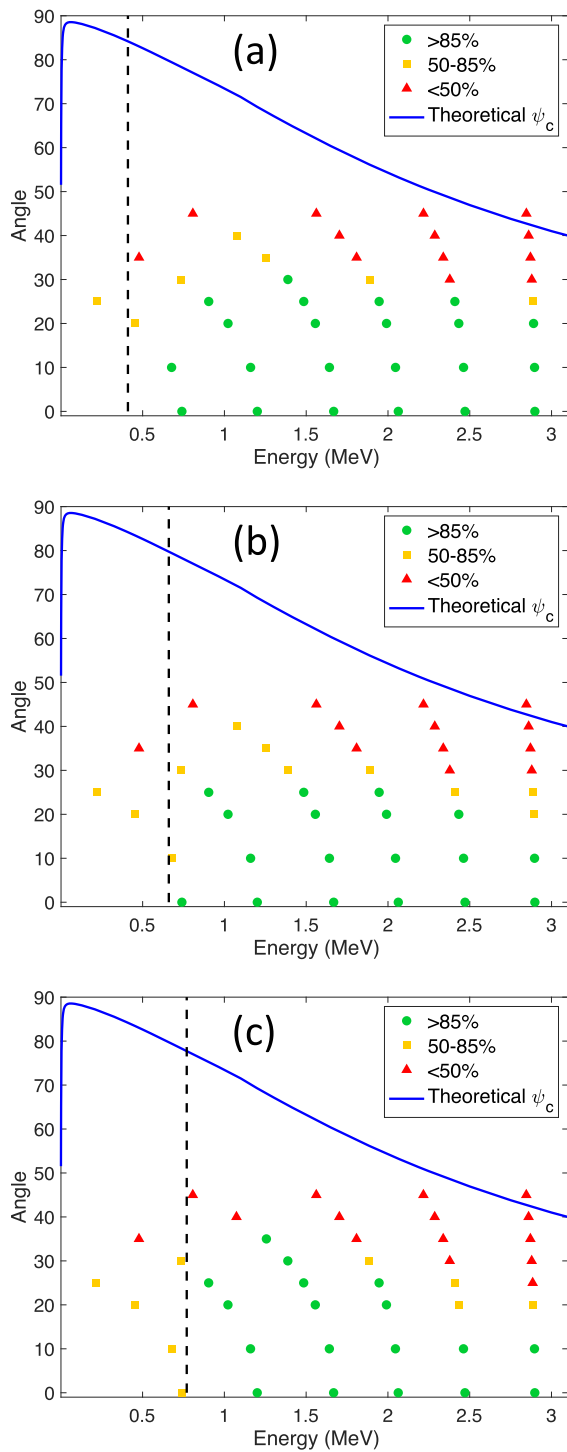


FIG. 7. Observed detection efficiency at 2 h (a), 4 h (b), and 5 h (c) etch times. Detection efficiencies are sorted into three groupings: >85%, 50%–85%, and <50%. The solid curve is the theoretical critical angle from Eq. (5). The dashed vertical line represents the energy threshold below which proton tracks would be etched away at the particular etch time.

groupings, the proton signal tracks are concentrated at a reasonably low contrast and are distinct from high contrast background noise. However, in cases where the proton tracks are high in contrast, they cannot be isolated from the background noise on the CR-39. A cutoff of contrast $\leq 50\%$ was imposed in our data analysis, as the resolving signal becomes increasingly difficult above this contrast level. Examples of both high contrast and low contrast cases are shown in Fig. 4. When the signal cannot be properly separated from noise, there is an additional source of error based on scans of background noise by Lahmann *et al.*¹²

An uncertainty figure is derived based on the observed error for the number of background tracks, shown across a sample of pieces in Fig. 5. We perform a background subtraction for the CR-39 piece and then use the remaining data to find the track yield. The fractional uncertainty on these resulting data scales linearly with the background uncertainty and inversely with the measured number of proton tracks, making the overall fractional error contribution equal to $\beta/\Phi_{\text{measured}}$, where β is the value of background uncertainty.

Summing this background noise uncertainty with the distance measurement uncertainty of 4% in quadrature, we obtain a relative uncertainty on the measured flux in CR-39,

$$\frac{\sigma}{n} = \sqrt{0.04^2 + \left(\frac{\beta}{\Phi_{\text{measured}}}\right)^2}. \quad (3)$$

IV. RESULTS

A. Detection efficiency

An initial overview of the CR-39 scan data reveals an upper limit on angled detection. Above 45° , no proton tracks can be resolved from background noise. We thus consider any offset of $\geq 45^\circ$ to be entirely impractical for any detector design.

Detection efficiency data from 0° to 30° with a 2 h etch are shown in Fig. 6. Additional plots for 4 h and 5 h etch times are shown in Appendix A. For angles through 25° , the detection

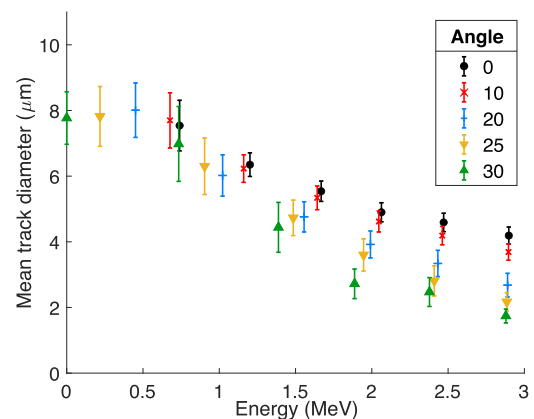


FIG. 8. Track diameter vs incident energy at 2 h etch time. Here, we see that tracks tend to get smaller as the incident angle gets larger. Error bars represent the standard deviation on the track diameter distribution.

efficiencies are within the error of one another between 1.0 MeV and 2.1 MeV. Moreover, the incident angle of 10° has no effect on detection efficiency for all data above 1.0 MeV, up through the highest energy filter.

Detection efficiency drops at 30° for all incident energies. Above 1.0 MeV, detection at 30° also decreases as energy increases, suggesting that the critical angle at which detection efficiency decreases as energy increases.

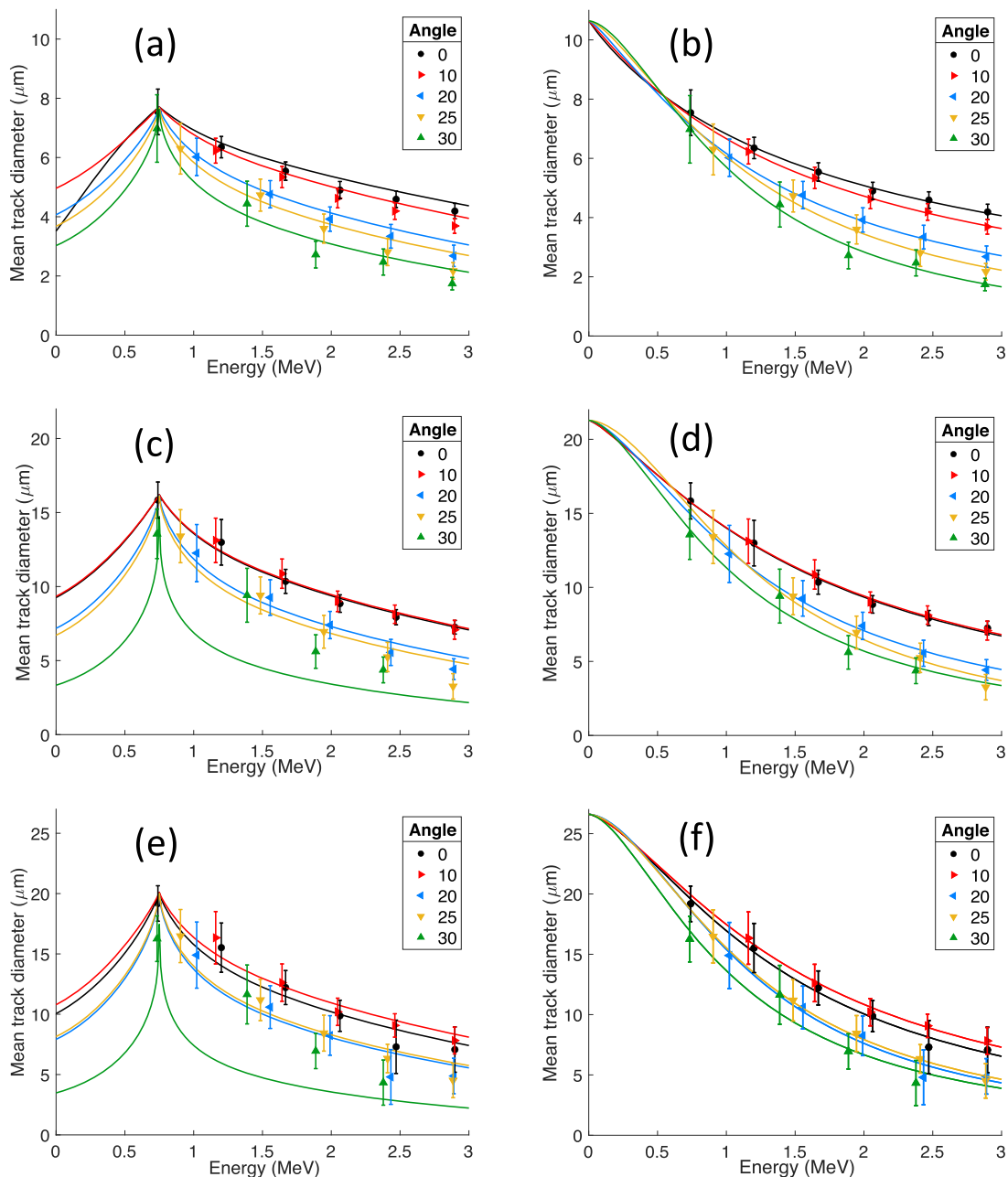


FIG. 9. Comparison of c-parameter and two-parameter fits of track diameter vs energy for non-normal incident protons. The left column of panels (a), (c), and (e) are the c-parameter fits for 2-h, 4-h, and 5-h etch times, respectively, and the right column of panels (b), (d), and (f) are two-parameter fits for 2-h, 4-h, and 5-h etch times, respectively. As with Fig. 8, the error bar size is one standard deviation on the track diameter distribution. Particularly for the 4 h and 5 h etch times, the two-parameter fit describes the data better at non-normal incidence.

Theoretical models of track formation in CR-39 define the critical angle as the incident angle at which the perpendicular track etch velocity \vec{V}_T is equal to the bulk etch velocity \vec{V}_B .⁸ Beyond this angle, no tracks are observed.

The track etch and bulk etch velocities in CR-39 can be modeled by the following empirical relation:

$$|\vec{V}_T| = |\vec{V}_B| \left(1 + k \left(\left[\frac{dE}{dx}(E) \right]_{\frac{\text{keV}}{\mu\text{m}}} \right)^n \right), \quad (4)$$

where E is the incident energy of the charged particle and $\frac{dE}{dx}(E)$ is the local stopping power in CR-39. The values of k and n are chosen to agree with the observed etch behavior:¹³ $k = 6 \times 10^{-5}$ and $n = 2.76$.

Equating the normal component of $|\vec{V}_T|$ with $|\vec{V}_B|$ gives us the following expression for the critical angle ψ_c :

$$\cos(\psi_c) = \left(1 + k \left(\left[\frac{dE}{dx}(E) \right]_{\frac{\text{keV}}{\mu\text{m}}} \right)^n \right)^{-1}. \quad (5)$$

In practice, the detection efficiency does not drop immediately from 100% to 0% past the critical angle due to multiple Coulomb scattering (straggling). The incident energy upon passing through aluminum filters is not a discrete value; rather, it is a distribution with non-negligible widths. The standard deviations on the mean energies for the six filters are given in Table I. Thus, we observe a detection dropoff that occurs continuously rather than discretely. Following the approach of Stafford *et al.*,⁸ we can extrapolate the critical angle, in practice, as the point of 50% detection efficiency.

We compare the theoretical critical angle to our experiment by plotting the detection efficiency as a function of energy and angle. Plots with three regions of detection efficiency (>85%, 50%–85%, and <50%) are shown in Fig. 7 along with the theoretical modeled critical angle from Eq. (5).

Experimental data show more limited regions of detection than those suggested by the critical angle theory. The modeled critical angle from Eq. (5) is higher than that observed from the 50% efficiency points. It also predicts detection at and above 50° for energies below 2.5 MeV. In our experiment, however, we observed no tracks at incident angles greater than 45°.

Moreover, the theory described in Eq. (5) suggests that the critical angle peaks at an incident energy of about 0.1 MeV and decreases monotonically with higher energy. However, the maximum critical angle is observed between 1.0 and 1.5 MeV. The critical angle then monotonically decreases beyond 1.5 MeV. We attribute the behavior below 1.0 MeV to low energy protons having a range in CR-39 that is shallower than the etch depth. As explored in calculations by Dörschel *et al.*,¹⁴ in the lower energy limits, these proton tracks are etched away and thus not observable. The energy threshold for the proton range to exceed the etch depth is plotted as a dashed vertical line in Fig. 7 for each etch time and is seen to agree with the efficiency dropoff at low energies. Reflecting this low energy effect, Dörschel *et al.* modeled the maximum

critical angle to occur at slightly higher energies as the etch time increases. These maxima shifts were calculated to be on the order of a few hundred keV. However, the limited energy and angle resolution of our experiment make this effect difficult to quantify experimentally.

B. Diameter-energy relationship

Proton tracks in CR-39 have a characteristic size that depends on the incident energy and etch times. The relation between the track diameter and energy is useful for experiments with step range filters (SRF),^{15,16} wedge range filters (WRF),^{5,17,18} and the aforementioned neutron spectrometer.¹⁰ The track diameter d is computed by the CR-39 scan system from the track area A by the expression $d = \sqrt{4A/\pi}$.

A plot of the average track diameter vs incident energy and angle is shown in Fig. 8. We observe that, beyond 1 MeV, the diameter decreases as the incident angle increases. This difference becomes more pronounced as the incident energy increases.

Two distinct models have been used to describe the relationship between the track diameter and incident energy at normal incidence. In the previous work of Lahmann *et al.*,¹³ modeling tracks etched in CR-39 demonstrated a relationship between track diameter D and incident energy E as follows:

$$D(E) = \frac{2\tau_E |\vec{V}_B|}{1 + k' \left(\frac{E_{\text{MeV}}}{Z^2 A} \right)^{n'}}, \quad (6)$$

where τ_E is the etch time, k' and n' are the two fit parameters, Z is the charge, and A is the atomic mass number. This diameter-energy relationship is dependent on two empirical fit parameters, k' and n' , and is thus referred to as the two-parameter model.

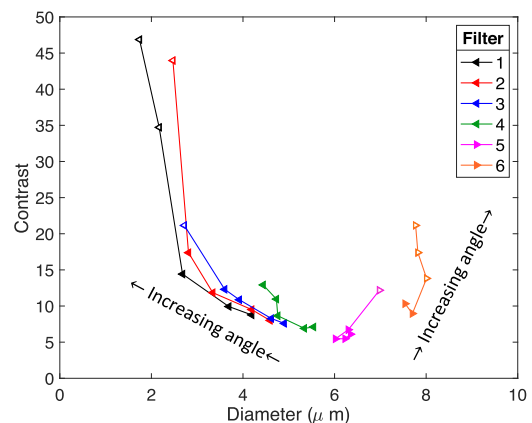


FIG. 10. Proton track contrast vs track diameter at 2 h etch time for each filter. The arrows indicate the direction of increasing angle. Solid data points indicate detection efficiencies >85% at the particular energy and incident angle, while hollow points indicate detection efficiencies below 85%.

A different diameter–energy model typically used for proton data is a larger set of equations that depends on one parameter, c , as well as a measured maximum diameter, D_{max} . This is known as the c -parameter model.¹³

Both the two-parameter and c -parameter models have been shown to work equally well for protons at normal incidence to CR-39. However, the use of these fitting models at non-normal incidence

has not previously been tested. Although one would not necessarily expect these models derived for normal incidence to extend to the non-normal cases, we can attempt to fit angled incidence data using these models.

The results of the fitting processes are shown in Fig. 9. The track diameter decreases as the incident angle increases. The two-parameter model fits the data noticeably better than the c -parameter

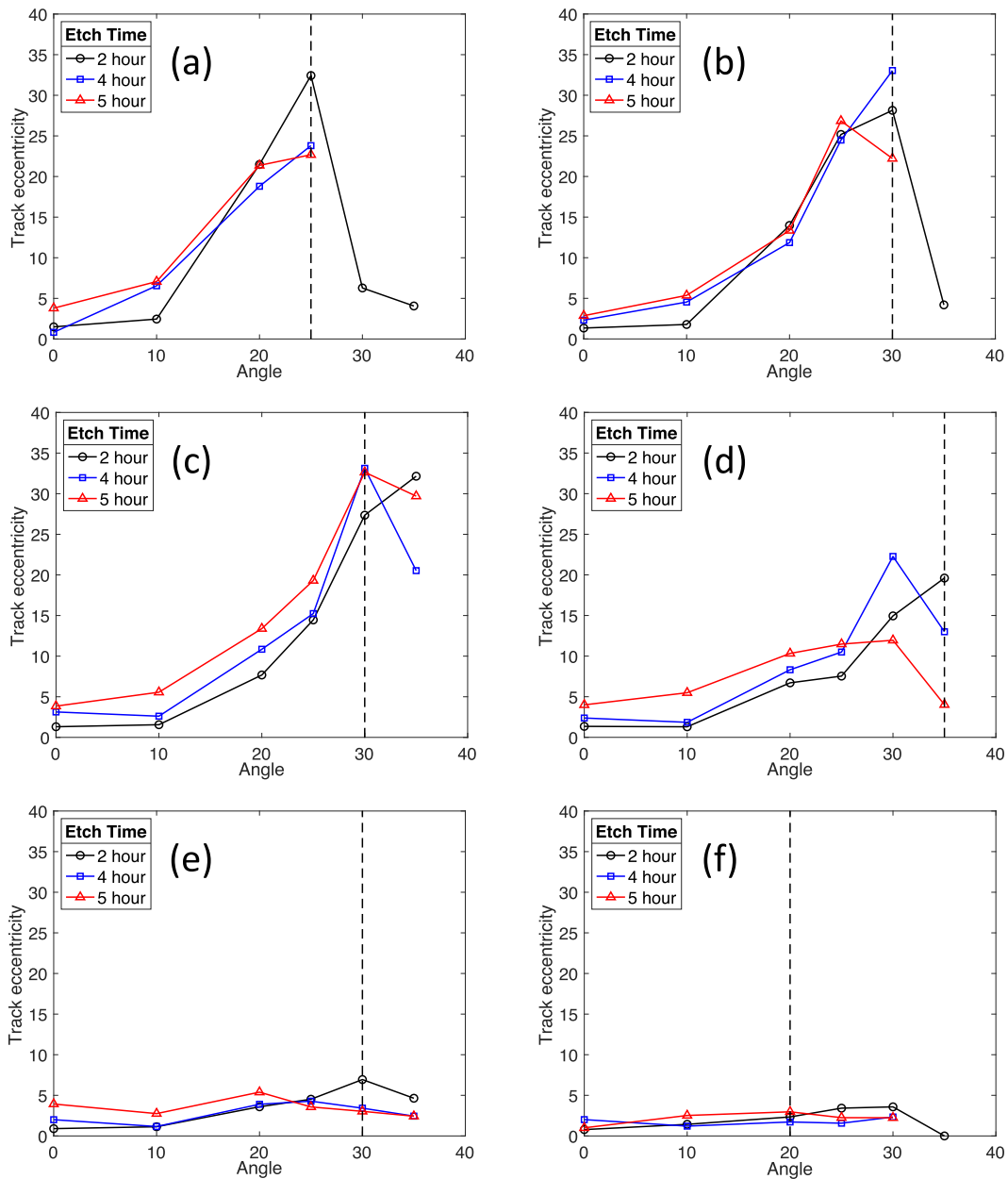


FIG. 11. Track eccentricity data for all filters at 2 h, 4 h, and 5 h etch times. Panels (a)–(f) plot data from filters 1–6, respectively. The dashed vertical line on each plot represents the extrapolated critical angle from the detection efficiency data.

model for incident angles $\geq 20^\circ$. The c-parameter fit increasingly deviates from the data for greater etch times.

From the diameter–energy fits, it is shown that the two-parameter model can be extended to non-normal incident protons by choosing appropriate fit parameters k' and n' . The c-parameter model with D_{max} reflecting a reasonable experimental maximum diameter does not accurately describe the data at higher angles.

C. Track contrast

The contrast of proton tracks is recorded by the microscope scanning system as a measure of the darkness of the track relative to the average darkness of the frame. A lower contrast indicates a darker track, and vice versa.

A plot of contrast vs track diameter is shown in Fig. 10. For the four highest energy filters, the diameter tends to decrease while contrast increases as the incident angle increases. The two lowest energy filters exhibit minimal variation in diameter but show an increase in contrast with the increasing angle.

The high contrast behavior of filters 1 and 2 at 30° suggests that the loss in detection efficiency (denoted by the hollow marker in Fig. 10) is at least somewhat attributable to the imposed contrast $\leq 50\%$ cutoff. With the mean contrast approaching 50%, it is likely that a significant portion of tracks are lost in the noise above 50% contrast.

D. Track eccentricity

The measure of track roundness is characterized by track eccentricity, which varies from 0% to 100%, with eccentricity 0% being a circular track. A detailed explanation of how eccentricity is computed is given by Seguin *et al.*⁵ In normal incidence experiments, tracks are expected to be nearly circular, so one can ignore tracks above a low eccentricity as background noise. However, in non-normal incidence experiments, we expect a typical track to be elongated, having a nonzero eccentricity. A better understanding of the eccentricity as a function of incidence angle is relevant for data processing of angled incidence applications.

The mean track eccentricity as a function of incidence angle is plotted in Fig. 11. As expected, the eccentricity increases with the incidence angle. The eccentricity also increases with energy, so the higher energy particles produce more eccentric tracks. At the lowest energy filter, shown in Fig. 11(f), the tracks remain nearly circular for all angles.

Also shown in Fig. 11 is the tendency for tracks to become more rounded beyond the critical angle. This is most pronounced at the higher energies shown in Figs. 11(a) and 11(b). An approximate critical angle is determined from the 50% detection efficiency points at 2 h, 4 h, and 5 h in Fig. 7. The pattern of eccentricity increasing with the angle remains up to the critical angle (denoted by the dashed vertical line in Fig. 11) at which point the eccentricity drops noticeably. The eccentricity drop correlates with the drop in detection efficiency, so we believe that this is an artificial effect arising from limited proton detection. This effect is difficult to probe further due to the lack of reliable data beyond the critical angle, where very few tracks are visible.

V. CONCLUSIONS

In this paper, we have examined the behavior of the nuclear track detector CR-39 in response to protons incident at an angle. These results are relevant for ICF applications that use CR-39 in configurations with non-normal incident charged particles. As a specific example, these data are essential for a recently proposed neutron spectrometer at the Z facility.

The study of detection efficiency at proton incident angles up to 50° offers a number of insights relevant for the spectrometer design. In the energy regime studied (< 3 MeV), angles beyond 45° produce no usable data. In general, incident angles $\geq 30^\circ$ had detection efficiencies well below 100% and were thus shown to be impractical for detector design. We propose a usable energy range between 1.0 MeV and 2.1 MeV for spectrometers involving proton incident angles up to 25° . This energy range can be extended up to 2.9 MeV for incident angles of 10° or less.

The detection efficiency experiments in this paper yield limitations on critical angle theory. The critical angle observed in the data is significantly lower than that predicted by the theory. The region of proton detection is thus far more limited than the critical angle theory predicts. A detection dropoff is also observed at the lowest energies, which is accounted for by predictions for the bulk etch depth vs proton range in CR-39. Low energy protons yield shallow tracks that can vanish during the etch process.

The track diameter vs energy relationship was studied for non-normal incidence protons. We found that the track diameter decreases with the increasing incident angle. Two fitting methods for the normal incidence case were discussed; the two-parameter model was shown to extend to angles above 20° , while the c-parameter model did not fit the data.

Contrast, a measure of track darkness, was studied in its relation to track diameter and energy. Contrast tends to increase with the angle, while the track diameter decreases. These effects are more pronounced for higher energies. At the two highest energies, the average contrast near 50% is proposed as a possible mechanism for the reduced detection efficiency at 30° incidence.

The track eccentricity, measuring roundness of the proton tracks, was found to increase as the incident angle increases. The rate of increase is greatest for higher energies, and the lowest energy tracks remain nearly circular.

ACKNOWLEDGMENTS

The authors sincerely thank Bob Frankel and Ernie Doeg for help with CR-39 processing. This material is based on the work supported by the Department of Energy, National Nuclear Security Administration (Award No. DE-NA0003868) and by Sandia National Laboratories (Contract No. 2080471). This report was prepared as an account of work sponsored by an agency of the United States Government. Neither the United States Government nor any agency thereof, nor any of their employees, makes any warranty, express or implied, or assumes any legal liability or responsibility for the accuracy, completeness, or usefulness of any information, apparatus, product, or process disclosed, or represents that its

use would not infringe privately owned rights. Reference herein to any specific commercial product, process, or service by trade name, trademark, manufacturer, or otherwise does not necessarily constitute or imply its endorsement, recommendation, or favoring by the United States Government or any agency thereof. The views and opinions of authors expressed herein do not necessarily state or reflect those of the United States Government or any agency thereof.

these plots illustrate the detection dropoff at low energies for higher etch times, which we have attributed to the shallow tracks being etched away.

APPENDIX A: DETECTION EFFICIENCY PLOTS

Plots similar to Fig. 6 were obtained for the 4 h and 5 h etch times, as shown in Fig. 12. In comparison to the 2 h etch time plot,

APPENDIX B: CONTRAST VS INCIDENT ANGLE

The track contrast data are plotted in Fig. 13 in the same manner as the eccentricity data from Fig. 11. The contrast tends to increase with the angle, with the rate of increase decreasing as the incident energy decreases. At the two lowest energies, the higher etch time (5 h) has a higher contrast. This can be attributed to tracks becoming lighter as they are nearly etched away at higher etch times.

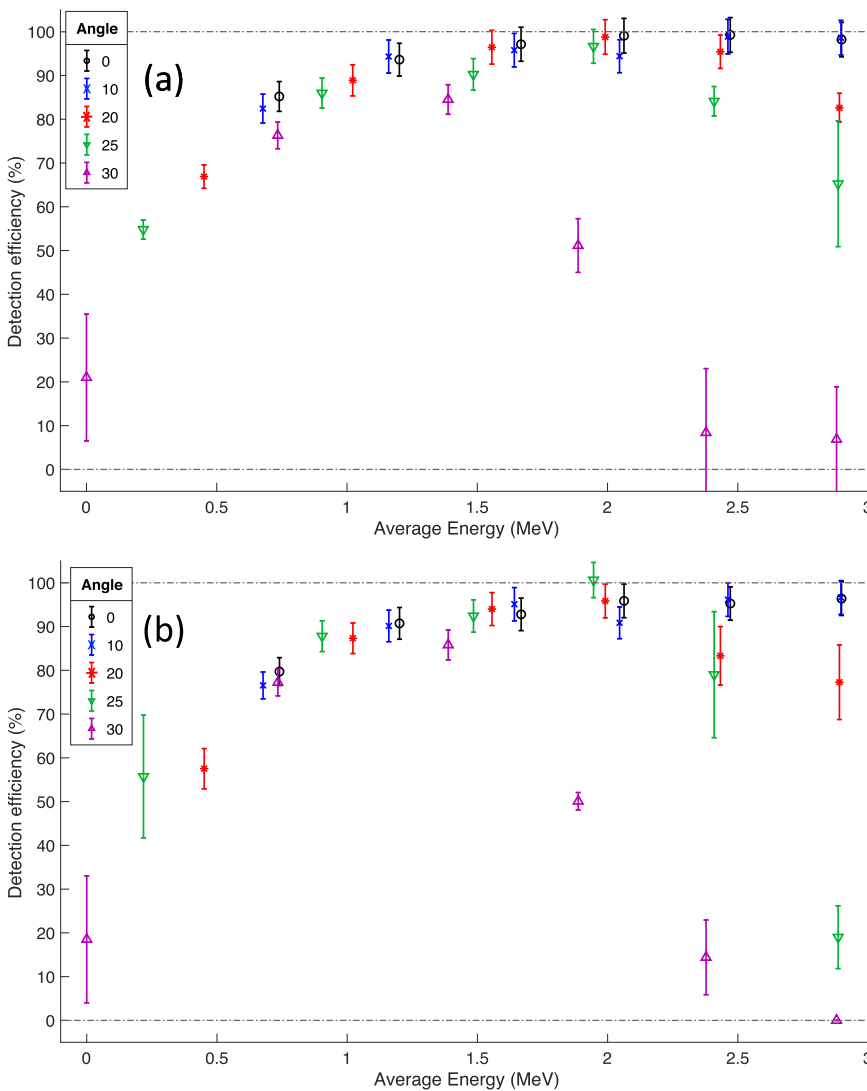


FIG. 12. Detection efficiency vs energy for 4 h and 5 h etch times in panels (a) and (b), respectively. The dropoff in detection at low energies due to tracks etched away is visible here in comparison to the 2 h etch time.

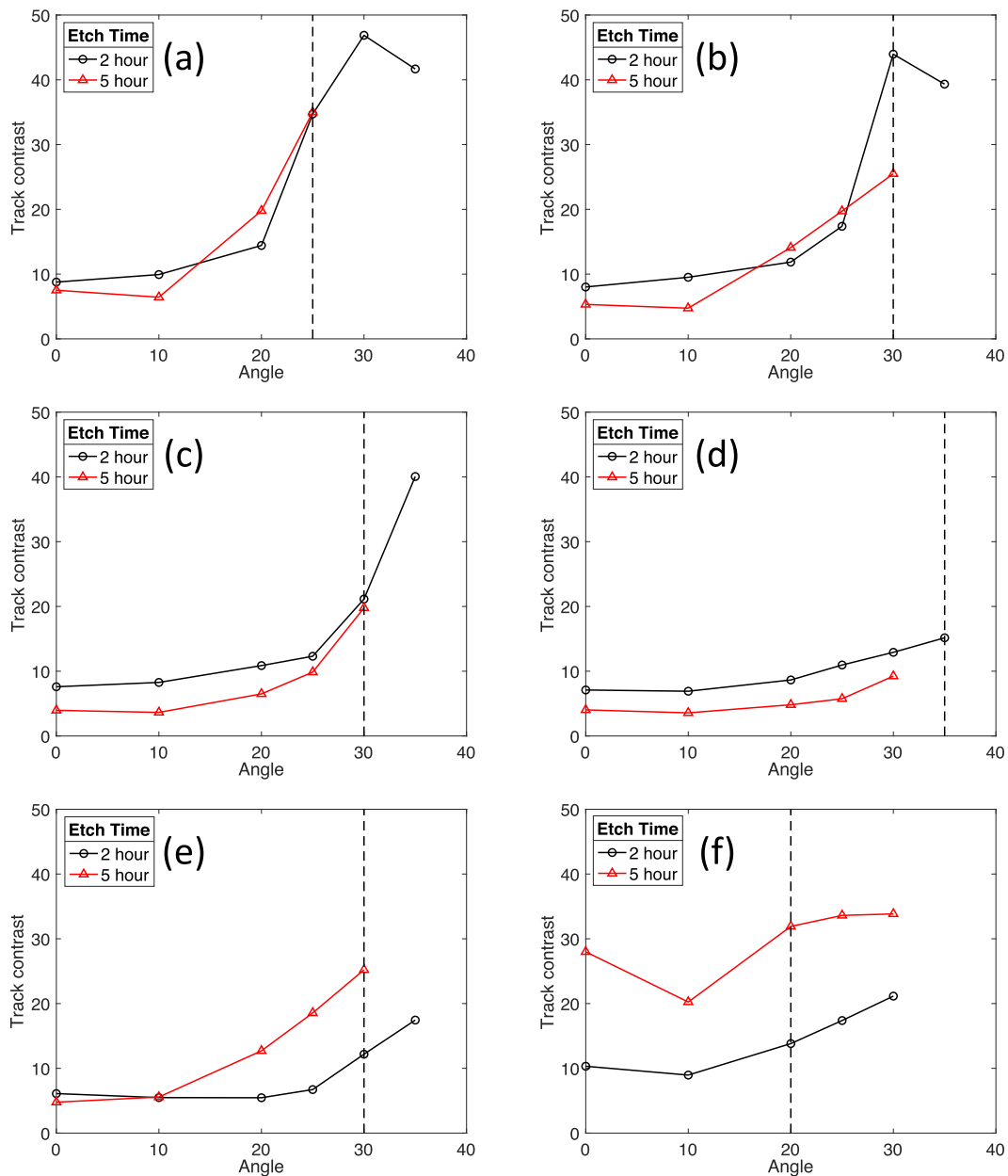


FIG. 13. Plots of track contrast vs incident angle for 2 h and 5 h etch times. Panels (a)–(f) plot data from filters 1–6, respectively. The dashed vertical line is the extrapolated critical angle for each filter. Contrast (how light the track is) tends to increase with the angle, which is more pronounced at the highest energy filters [(a) and (b)].

DATA AVAILABILITY

The data that support the findings of this study are available from the corresponding author upon reasonable request.

REFERENCES

¹T. R. Boehly, D. L. Brown, R. S. Craxton, R. L. Keck, J. P. Knauer, J. H. Kelly, T. J. Kessler, S. A. Kumpan, S. J. Loucks, S. A. Letzring, F. J. Marshall, R. L. McCrory,

S. F. B. Morse, W. Seka, J. M. Soares, and C. P. Verdon, *Opt. Commun.* **133**, 495 (1997).

²M. Cuneo, M. C. Herrmann, D. B. Sinars, S. A. Slutz, W. A. Stygar, R. A. Vesey, A. B. Sefkow, G. A. Rochau, G. A. Chandler, J. E. Bailey, J. L. Porter, R. D. McBride, D. C. Rovang, M. G. Mazarakis, E. P. Yu, D. C. Lamppa, and K. J. Peterson, *IEEE Trans. Plasma Sci.* **40**(12), 3222 (2012).

³G. H. Miller, E. I. Moses, and C. R. Wuest, *Nucl. Fusion* **44**, S228 (2004).

⁴S. A. Durrani and R. K. Bull, *Solid State Nuclear Track Detections, Principles, Methods and Applications* (Pergamon, New York, 1987).

- ⁵F. H. Séguin, J. A. Frenje, C. K. Li, D. G. Hicks, S. Kurebayashi, J. R. Rygg, B.-E. Schwartz, R. D. Petrasso, S. Roberts, J. M. Soares, D. D. Meyerhofer, T. C. Sangster, J. P. Knauer, C. Sorce, V. Y. Glebov, C. Stoeckl, T. W. Phillips, R. J. Leeper, K. Fletcher, and S. Padalino, *Rev. Sci. Instrum.* **74**, 975 (2003).
- ⁶D. Hermsdorf, *Radiat. Meas.* **46**, 396 (2011).
- ⁷B. Dörschel, D. Fülle, H. Hartmann, D. Hermsdorf, K. Kadner, and Ch. Radlach, *Radiat. Prot. Dosim.* **71**(2), 99 (1997).
- ⁸P. M. Stafford, J. L. Horton, K. R. Hogstrom, P. M. DeLuca, Jr., and D. Holslin, *Nucl. Tracks Radiat. Meas.* **14**, 373 (1988).
- ⁹J. A. Frenje, C. K. Li, F. H. Séguin, D. G. Hicks, S. Kurebayashi, R. D. Petrasso, S. Roberts, V. Y. Glebov, D. D. Meyerhofer, T. C. Sangster, J. M. Soares, C. Stoeckl, C. Chiritescu, G. J. Schmid, R. A. Lerche, and R. A. Lerche, *Rev. Sci. Instrum.* **73**, 2597 (2002).
- ¹⁰B. Lahmann, M. Gatu Johnson, K. D. Hahn, J. A. Frenje, D. J. Ampleford, B. Jones, M. A. Mangan, A. Maurer, C. L. Ruiz, F. H. Séguin, and R. D. Petrasso, *Rev. Sci. Instrum.* **91**, 073501 (2020).
- ¹¹N. Sinenian, M. J.-E. Manuel, A. B. Zylstra, M. Rosenberg, C. J. Waugh, H. G. Rinderknecht, D. T. Casey, H. Sio, J. K. Rusczyński, L. Zhou, M. G. Johnson, J. A. Frenje, F. H. Séguin, C. K. Li, R. D. Petrasso, C. L. Ruiz, and R. J. Leeper, *Rev. Sci. Instrum.* **83**, 043502 (2012).
- ¹²B. Lahmann, “First CR-39 D-D neutron calibrations on the Z facility,” *Rev. Sci. Instrum.* (unpublished).
- ¹³B. Lahmann, M. Gatu Johnson, J. A. Frenje, Y. Y. Glebov, H. G. Rinderknecht, F. H. Séguin, G. Sutcliffe, and R. D. Petrasso, *Rev. Sci. Instrum.* **91**, 053502 (2020).
- ¹⁴B. Dörschel, D. Fülle, H. Hartmann, D. Hermsdorf, K. Kadner, and Ch. Radlach, *Radiat. Prot. Dosim.* **71**(4), 245 (1997).
- ¹⁵B. Lahmann, M. Gatu Johnson, J. A. Frenje, A. J. Birkel, P. J. Adrian, N. Kabadi, J. H. Kunimune, T. M. Johnson, J. A. Percy, B. L. Reichelt, F. H. Seguin, G. Sutcliffe, and R. D. Petrasso, “Extension of charged-particle spectrometer capabilities for diagnosing implosions on OMEGA, Z, and the NIF,” *Rev. Sci. Instrum.* (unpublished).
- ¹⁶M. J. Rosenberg, A. B. Zylstra, J. A. Frenje, H. G. Rinderknecht, M. Gatu Johnson, C. J. Waugh, F. H. Séguin, H. Sio, N. Sinenian, C. K. Li, R. D. Petrasso, V. Y. Glebov, M. Hohenberger, C. Stoeckl, T. C. Sangster, C. B. Yeaman, S. LePape, A. J. Mackinnon, R. M. Bionta, B. Talison, D. T. Casey, O. L. Landen, M. J. Moran, R. A. Zacharias, J. D. Kilkenny, and A. Nikroo, *Rev. Sci. Instrum.* **85**, 103504 (2014).
- ¹⁷F. H. Seguin, N. Sinenian, M. Rosenberg, A. Zylstra, M. J.-E. Manuel, H. Sio, C. Waugh, H. G. Rinderknecht, M. G. Johnson, J. Frenje, C. K. Li, R. Petrasso, T. C. Sangster, and S. Roberts, *Rev. Sci. Instrum.* **83**, 10D908 (2012).
- ¹⁸A. B. Zylstra, J. A. Frenje, F. H. Séguin, M. J. Rosenberg, H. G. Rinderknecht, M. G. Johnson, D. T. Casey, N. Sinenian, M. J.-E. Manuel, C. J. Waugh, H. W. Sio, C. K. Li, R. D. Petrasso, S. Friedrich, K. Knittel, R. Bionta, M. McKernan, D. Callahan, G. W. Collins, E. Dewald, T. Döppner, M. J. Edwards, S. Glenzer, D. G. Hicks, O. L. Landen, R. London, A. Mackinnon, N. Meezan, R. R. Prasad, J. Ralph, M. Richardson, J. R. Rygg, S. Sepke, S. Weber, R. Zacharias, E. Moses, J. Kilkenny, A. Nikroo, T. C. Sangster, V. Glebov, C. Stoeckl, R. Olson, R. J. Leeper, J. Kline, G. Kyrala, and D. Wilson, *Rev. Sci. Instrum.* **83**, 10D901 (2012).